The Journal of Chemical Physics

Intrinsic dissipation mechanisms in metallic glass resonators

Cite as: J. Chem. Phys. **151**, 144506 (2019); https://doi.org/10.1063/1.5116895
Submitted: 29 June 2019 . Accepted: 24 September 2019 . Published Online: 11 October 2019

Meng Fan, Aya Nawano, Jan Schroers, Mark D. Shattuck, and Corey S. O'Hern

The Journal of Chemical Physics ARTICLE scitation.org/journal/jcp

Intrinsic dissipation mechanisms in metallic glass resonators

Cite as: J. Chem. Phys. 151, 144506 (2019); doi: 10.1063/1.5116895
Submitted: 29 June 2019 • Accepted: 24 September 2019 •
Published Online: 11 October 2019

Meng Fan,[1,2] Aya Nawano,[1,2] Jan Schroers,[1,2] Mark D. Shattuck,[1,3] and Corey S. O'Hern[1,2,4,5,a)]

AFFILIATIONS

[1]Department of Mechanical Engineering and Materials Science, Yale University, New Haven, Connecticut 06520, USA
[2]Center for Research on Interface Structures and Phenomena, Yale University, New Haven, Connecticut 06520, USA
[3]Department of Physics and Benjamin Levich Institute, The City College of the City University of New York, New York, New York 10031, USA
[4]Department of Physics, Yale University, New Haven, Connecticut 06520, USA
[5]Department of Applied Physics, Yale University, New Haven, Connecticut 06520, USA

[a)]**Electronic mail:** corey.ohern@yale.edu

ABSTRACT

Micro- and nanoresonators have important applications including sensing, navigation, and biochemical detection. Their performance is quantified using the quality factor Q, which gives the ratio of the energy stored to the energy dissipated per cycle. Metallic glasses are a promising material class for micro- and nanoscale resonators since they are amorphous and can be fabricated precisely into complex shapes on these length scales. To understand the intrinsic dissipation mechanisms that ultimately limit large Q-values in metallic glasses, we perform molecular dynamics simulations to model metallic glass resonators subjected to bending vibrations at low temperatures. We calculate the power spectrum of the kinetic energy, redistribution of energy from the fundamental mode of vibration, and Q vs the kinetic energy per atom K of the excitation. In the harmonic and anharmonic response regimes where there are no atomic rearrangements, we find that $Q \to \infty$ over the time periods we consider (since we do not consider coupling to the environment). We identify a characteristic K_r above which atomic rearrangements occur, and there is significant energy leakage from the fundamental mode to higher frequencies, causing finite Q. Thus, K_r is a critical parameter determining resonator performance. We show that K_r decreases as a power-law, $K_r \sim N^{-k}$, with increasing system size N, where $k \approx 1.3$. We estimate the critical strain $\langle \gamma_r \rangle \sim 10^{-8}$ for micrometer-sized resonators below which atomic rearrangements do not occur in the millikelvin temperature range, and thus, large Q-values can be obtained when they are operated below γ_r. We also find that K_r for amorphous resonators is comparable to that for resonators with crystalline order.

I. INTRODUCTION

Micro- and nanoresonators have numerous important applications including navigation, sensing, chemical detection, molecular separation, and biological imaging.[1] The performance of resonators is typically measured by the quality factor, Q, which gives the ratio of the energy stored to the energy dissipated per cycle in the resonator during operation.[2] Micro- and nanoresonators made from nonmetallic crystalline materials, such as sapphire,[3] carbon nanotubes,[4,5] and single-crystal diamond,[6] can possess quality factors $Q > 10^6$ at low temperatures. However, it is difficult to fabricate these materials into complex shapes, and many applications require electrical conduction. As a result, crystalline metals are used in many resonator applications, yet they suffer from energy losses that arise from topological defects and grain boundaries.[7]

In an effort to obviate energy losses from topological defects and grain boundaries that occur in crystalline metals, as well as take advantage of their plastic-forming ability to be fabricated into complex shapes, several groups have considered resonators made from metallic glasses (MGs).[8–12] MGs are cooled rapidly to avoid crystallization, and thus, they possess uniformly disordered structure. Recent experiments have shown that metallic-glass-based resonators can achieve quality factors that are comparable

and even larger than those for resonators made from crystalline metals.[9,13,14] Metallic glasses offer the additional benefit for resonator applications in that they can be thermoplastically formed into complex shapes with spatial features that span many orders of magnitude.[15–17]

In this work, we analyze the mechanisms that give rise to dissipation in model glasses, which will allow us to better understand why metallic glass resonators possess finite quality factor at very low temperatures. The mechanisms that give rise to energy losses in resonators during vibration can be classified as intrinsic or extrinsic.[1] Extrinsic losses, such as anchoring and frictional losses, come from interactions between the resonator and its surrounding environment.[18,19] In contrast, intrinsic losses originate from flaws or defects within the resonator, such as dislocations, grain boundaries, vacancies, and interstitials in crystalline materials. In metallic glasses, which lack crystalline order, intrinsic losses are envisioned to stem from irreversible, collective atomic rearrangements, or shear-transformation zones (STZs).[20] A number of studies have characterized the role of collective atomic rearrangements in determining the mechanical properties of metallic glasses, including ductility, yielding, and shear-band formation.[21–25]

Internal friction measurements have been performed to gain insight into intrinsic dissipation mechanisms and the quality factor of metallic glasses.[7,26,27] However, a key focus in this work has been on revealing structural relaxation processes at elevated temperatures (i.e., near the glass transition temperature), rather than their low-temperature behavior. In these studies, metallic glass samples are typically perturbed by mechanical or electrostatic excitation using a torsion pendulum or dynamical mechanical analyzer, and the internal friction is measured as a function of temperature, frequency, and strain amplitude.[7,28,29] The internal friction, which is proportional to Q^{-1}, is generally small for temperatures below room temperature and then increases dramatically, forming a strong peak at temperatures typically above 400–500 K due to collective α structural relaxations.[8,30,31] Studies[7] have also reported a much smaller peak (typically four orders of magnitude smaller than that corresponding to α relaxations) in the internal friction of metallic glasses between 50 K and room temperature. Researchers have suggested that this peak corresponds to localized, anelastic so-called β relaxations. Explanations of the peaks in the internal friction include the creation and destruction of free volume,[32] dislocation motion,[33] shear transformation zones,[20] shear bands, and other mechanisms that involve structural rearrangements. At even lower temperatures (<50 K), the internal friction has been described using the quantum mechanical tunneling model for two-level systems.[34,35]

Most of these prior studies of the vibrational properties of metallic glasses either use a quantum mechanical approach for the low-temperature behavior or consider temperatures near room temperature and above, where thermal fluctuations are significant and microscopic rearrangements of atoms are frequent. In this work, we will take a different but still classical approach and focus on the nearly zero-temperature regime, where even microscopic rearrangements of atoms are rare, to better understand the transition from the harmonic response regime where Q is infinite over the time periods we consider (since we do not consider coupling of the system to the environment) to the highly anharmonic regime where Q becomes finite.

Our work is also related to studies of energy equipartition in weakly nonlinear spring networks. In the original work of Fermi, Pasta, and Ulam (FPU)[36] and in the subsequent work that considered larger systems and longer time scales,[37–40] the authors considered one-dimensional lattices of masses connected by nonlinear springs and investigated the extent to which energy input into a single or a few eigenmodes of the system can be transferred to other modes during vibration and whether these weakly anharmonic systems can reach thermal equilibrium with equipartition of energy among all of the eigenmodes. These studies have also been extended to two-[41,42] and three-dimensional systems with a variety of interparticle potentials.[43–45] This body of prior work is similar to ours in this sense that we input a single low-frequency eigenmode into an anharmonic system and study the transfer of energy out of the original eigenmode. However, there are key differences between this body of work and our current studies. Most importantly, in the systems we consider, the atoms have finite range interactions (that become zero beyond a given interatomic separation specified by the atom size) and thus, the atoms can rearrange and change neighbors. To rearrange, the system must overcome a potential energy barrier, which induces strong anharmonicities into the system. In contrast, most prior studies of the approach to equipartition have focused on systems in which the interactions enforce that the particles do not rearrange. The potential energy landscape in such systems is much smoother than that for systems in which the particles can rearrange. Below, we will compare the vibrational response for anharmonic systems that experience atomics rearrangements and those that do not.

Here, we carry out molecular dynamics (MD) simulations to quantify the intrinsic dissipation caused by atomic rearrangements and measure the quality factor in model metallic glass resonators at low temperatures. We induce vibrations in a thin bar-shaped resonator by exciting the mode corresponding to the resonator's fundamental frequency with a given kinetic energy per atom K and then running MD at constant total energy. When K is small, i.e., $K < K_{nl}$, the resonator displays harmonic response, the spectrum of the vibrational modes only includes the fundamental mode, and $Q \to \infty$ over the time period we consider. For intermediate K, i.e., $K_{nl} < K < K_r$, energy leaks to modes other than the fundamental mode, but at sufficiently long times, the leakage stops. Thus, in this regime, $Q \to \infty$ at the longest times we consider. For $K > K_r$, the system undergoes one or more atomic rearrangements, which induce strong dissipation and finite Q. Thus, the magnitude of K_r controls the performance of metallic glass resonators. We further show that K_r can be increased by decreasing the system size or by decreasing the cooling rate used to prepare the resonator. We also show that resonators with amorphous structure can achieve comparable performance (e.g., same Q) to those with partial crystalline order.

The remainder of the article is organized as follows. In Sec. II, we describe the simulation methods we use to prepare and excite the metallic glass resonators and to quantify the energy loss and quality factor of the vibrations. In Sec. III, we present the results, including measurements of the intrinsic loss and dissipation arising from anharmonicity of the potential and atomic rearrangements, techniques to increase Q by decreasing the system size and cooling rate, and comparisons of resonator performance in amorphous and crystalline samples. In Sec. IV, we summarize our findings and

present promising directions for future research. We also include four appendices. In Appendix A, we discuss the structure of the low-frequency eigenmodes. In Appendix B, we show that our results for the vibrational response do not depend strongly on the length of the time series of the vibrations that we collect. In Appendix C, we show the time dependence of the power spectrum of the kinetic energy, which supports the findings presented in the main text. In Appendix D, we compare the vibrational response for a thin-bar resonator with Lennard-Jones-like interactions and the response for a thin-bar resonator composed of a nonlinear spring network where atomic rearrangements are absent.

II. MODELS AND METHODS

We perform molecular dynamics (MD) simulations of binary Lennard-Jones mixtures using the Kob-Andersen model,[46] which has been employed to describe NiP alloys. Spherical atoms interact pairwise via the shifted-force version of the Lennard-Jones potential, $u(r_{ij}) = 4\varepsilon_{ij}[(\sigma_{ij}/r_{ij})^{12} - (\sigma_{ij}/r_{ij})^{6}]$ with a cutoff distance of $r_c = 2.5\sigma_{ij}$, where r_{ij} is the separation between atoms i and j. The total potential energy per atom is $U = N^{-1}\sum_{i>j}u(r_{ij})$. 80% of the atoms are type A ($N_A/N = 0.8$) and 20% are type B ($N_B/N = 0.2$), where $N = N_A + N_B$ is the total number of atoms, and the energy and length parameters are given by $\varepsilon_{AA} = 1.0$, $\varepsilon_{BB} = 0.5$, $\varepsilon_{AB} = 1.5$, $\sigma_{AA} = 1.0$, $\sigma_{BB} = 0.88$, and $\sigma_{AB} = 0.8$. All atoms have the same mass m. The energy, length, and pressure scales are given in terms of ε_{AA}, σ_{AA}, and $\varepsilon_{AA}/\sigma_{AA}^3$, respectively.

We initially placed the N atoms on an face-centered cubic (fcc) lattice in a long, thin box with aspect ratio L_x:L_y:L_z = 6:1:2 and periodic boundaries in the x-, y-, and z-directions at reduced number density $\rho = 1.0$. We then equilibrated the system at high temperature $T_0 > T_g \sim 0.4$[47] (which melts the crystal) by running molecular dynamics simulations at fixed number of atoms, pressure, and temperature (NPT) using the Nosé-Hoover thermostat with temperature $T_0 = 0.6$ and pressure $P_0 = 0.025$, a modified velocity-Verlet integration scheme, and time step $\Delta\bar{t} = 10^{-3}$. We then cool the system into a glassy state at zero temperature using a linear cooling ramp with time $\bar{t}$ such that $T(\bar{t}) = T_0 - R\bar{t}$. [The cooling rate is measured in units of $\varepsilon_{AA}^{3/2}/(m^{1/2}\sigma_{AA})$, where the Boltzmann constant $k_B = 1$.] We varied the cooling rate R over more than three orders of magnitude, yet we ensured that R was larger than the critical cooling rate R_c to avoid crystallization. The lowest cooling rates correspond to $\sim 10^{10}$ K/s, which is several orders of magnitude higher than the cooling rates that are typically achieved in experimental studies. Thus, the glasses we consider in simulations are not as energetically relaxed as those in experiments. However, the results concerning the effects of atomic rearrangements on the vibrational response are general and apply to samples generated over a wide range of cooling rates. We vary N from 250 to 8000 atoms to assess the finite size effects.

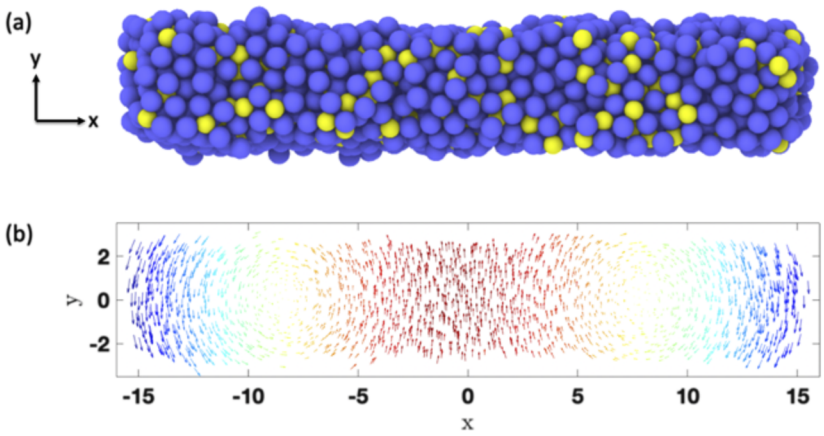

FIG. 1. (a) View of the model metallic glass resonator along the z axis. The bar contains $N = 2000$ atoms with aspect ratio L_x:L_y:L_z = 6:1:2. Blue and yellow atoms indicate A and B atom types, respectively. (b) Vector field representing the fundamental mode of the dynamical matrix of the metallic glass resonator in (a). The color scale highlights the y-component of the fundamental mode contribution for each atom with red corresponding to positive and blue corresponding to negative y-values.

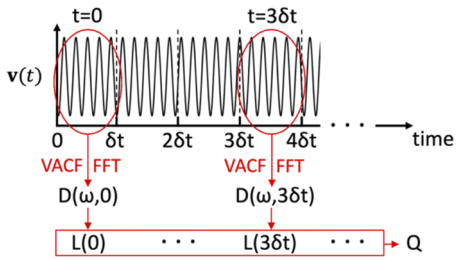

FIG. 2. Schematic diagram that illustrates the method we use to calculate the loss L and quality factor Q of model metallic glass resonators. We track the velocities **v** of the atoms in the resonator over a long time period. The time series is broken up into 20 time intervals with equal duration δt. We calculate the velocity autocorrelation function (VACF) for each time interval and fast Fourier transform (FFT) it to measure the power spectrum of the kinetic energy (at time t) $D(\omega, t)$ and loss $L(t)$ for each time interval t. Using Eq. (3), we can calculate the quality factor Q from $L(t)$.

After cooling the system to zero temperature, we remove the periodic boundary conditions in the x-, y-, and z-directions (creating free surfaces) and then apply conjugate gradient energy minimization to yield the zero-temperature configuration of the resonator, $\mathbf{R}_0 = \{x_1, y_1, z_1, \ldots, x_N, y_N, z_N\}$ [see Fig. 1(a) and Appendix A for visualizations of the eigenmodes for aspect ratios]. To induce vibrations, we excite the fundamental mode, i.e., the lowest eigenfrequency ω_1 of the dynamical matrix,[48] evaluated at $\mathbf{R}_0$ [see Fig. 1(b)]. The elongated, thin shape of the resonator guarantees that the lowest eigenfrequency is well-separated from higher ones. We then set the initial velocities of the atoms such that $\mathbf{v} = \{v_{x1}, v_{y1}, v_{z1}, \ldots, v_{xN}, v_{yN}, v_{zN}\} = \delta\mathbf{e}_1$, where $\mathbf{e}_1$ is the eigenvector corresponding to ω_1 and $\delta = \sqrt{2NK/m}$, and run MD simulations at constant total energy for a given time $t = \omega_1 \bar{t}/2\pi$. (The eigenvectors are normalized such that $\mathbf{e}_i \cdot \mathbf{e}_j = \delta_{ij}$, where δ_{ij} is the Kronecker delta and $i, j = 1, \ldots, 3N - 6$ are the indexes of the eigenvectors that correspond to the nontrivial eigenfrequencies.)

We track the atom positions and velocities over long time periods $t > 2700$ during the MD simulations. We then divide the long time series into 20 time intervals with equal duration $\delta t = 135$. We characterize the vibrational response of the system using two methods. In the first, we determine the vibrational response using the time period from 0 to δt. For the second method, we quantify how the vibrational response varies in time following the initial perturbation using a fixed tape length δt for each time interval. (We show that our results do not depend strongly on tape length δt in Appendix B.)

For each time interval between t to $t + \delta t$, we calculate the Fourier transform of the velocity autocorrelation function to determine the power spectrum of the kinetic energy (at time t) $D(\omega, t)$,[49]

$$D(\omega, t) = \int_0^{\delta t} \langle \mathbf{v}(t_0 + \tau) \cdot \mathbf{v}(t_0) \rangle_t e^{i\omega\tau} d\tau, \tag{1}$$

where ω is the angular frequency and $\langle \cdot \rangle_t$ indicates an average over all atoms and time origins t_0 between t and $t + \delta t$. See Fig. 2 for a summary of this approach.

For each time interval, we also determine the fraction of the kinetic energy that has transferred from the fundamental mode (with frequency ω_1) to other frequencies by defining the loss,

$$L(t) = 1 - \frac{\int_{\omega_1 - \Delta\omega}^{\omega_1 + \Delta\omega} D(\omega, t) d\omega}{\int_0^{\infty} D(\omega, t) d\omega}, \tag{2}$$

where $\Delta\omega = (\omega_2 - \omega_1)/2$ [see Fig. 3(b)]. By determining the loss $L(t)$ over consecutive time intervals, we can calculate the quality factor

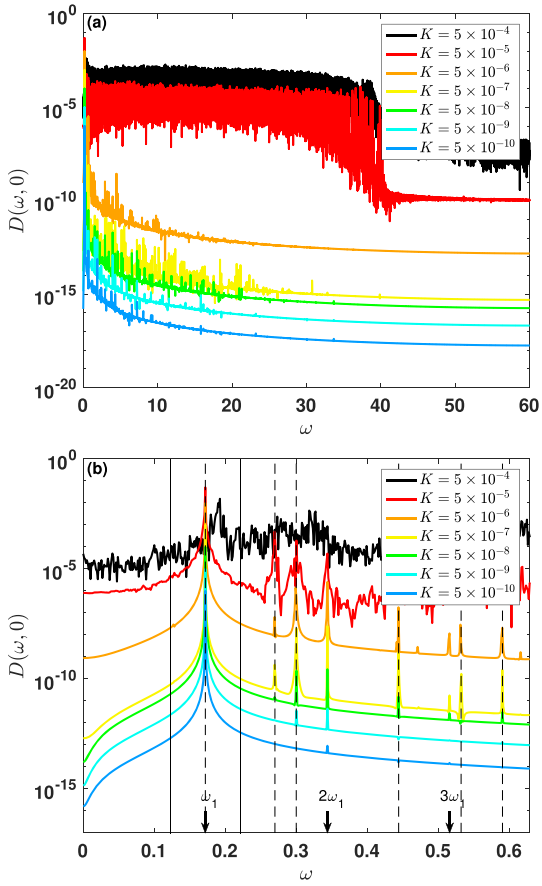

FIG. 3. (a) The power spectrum of the kinetic energy $D(\omega, 0)$ for the time interval $t = 0$ as a function of the kinetic energy per atom K. (b) $D(\omega, 0)$ for the same systems in (a), but a close-up of the low frequency regime. The vertical dashed lines indicate the vibrational frequencies $(\omega_1, \omega_2, \ldots, \omega_{3N-6})$ calculated from the dynamical matrix. The arrows indicate integer multiples of the fundamental frequency ω_1, and the two vertical solid lines show the region of frequencies near ω_1 used in Eq. (2) to calculate the loss.

$$Q = \omega_1 \left(\frac{dL(t)}{dt} \right)^{-1}. \tag{3}$$

Note that the results do not depend strongly on the magnitude of $\Delta\omega$ as long as it brackets ω_1.

To track the atomic displacements during vibration, we will also calculate the root-mean-square deviation (RMSD) between two configurations, e.g., $\mathbf{R}(t_1)$ and $\mathbf{R}(t_2)$ at different times t_1 and t_2,

$$d(\mathbf{R}(t_1), \mathbf{R}(t_2)) = \sqrt{N^{-1} \sum_{i=1}^{N} (x_i(t_1) - x_i(t_2))^2 + (y_i(t_1) - y_i(t_2))^2 + (z_i(t_1) - z_i(t_2))^2}, \tag{4}$$

where the sum is over all atoms.

III. RESULTS

The results are organized into three sections. In Sec. III A, we quantify the power spectrum of the kinetic energy $D(\omega, 0)$ and loss $L(0)$ during the first time interval ($t = 0$) as a function of the initial kinetic energy per atom K and investigate the effects of atomic rearrangements on the vibrational response. We also study the dependence of $D(\omega, t)$ and $L(t)$ on the time interval t and calculate the quality factor Q. We identify three characteristic regimes for vibrational response as a function of K: the harmonic response regime, where there is no leakage of energy from the fundamental mode to others, the anharmonic regime, where energy leakage occurs at short times, but it stops at long times, and the strong loss regime where atomic rearrangements occur, causing large losses and small Q. In Sec. III B, we investigate how variations of the system size N and cooling rate R affect the frequency of atomic rearrangements and thus the vibrational response. In Sec. III C, we calculate the loss in resonators made from polycrystalline and defected crystalline materials and compare it to resonators made from amorphous materials. We find that the losses generated from resonators with amorphous structure are comparable to that for crystalline resonators, which suggests that glassy materials may be promising for high-Q resonator applications.

A. Intrinsic dissipation: Anharmonicity and atomic rearrangements

We first focus on model metallic glass resonators with $N = 2000$ generated using cooling rate $R = 10^{-2}$. In Fig. 3, we show the power spectrum of the kinetic energy $D(\omega, 0)$ during the first time interval $t = 0$ after exciting the system along the fundamental mode as a function of the kinetic energy per atom over six orders of magnitude from $K = 5 \times 10^{-10}$ to 5×10^{-4}. When K is small, most of the response remains in the fundamental mode, ω_1, indicating that the system is in the harmonic response regime. As K increases, energy begins to leak to other modes of the dynamical matrix [indicated by the dashed vertical lines in Fig. 3(b)], as well as harmonics of the fundamental mode [indicated by the arrows in Fig. 3(b)]. The leakage of energy from the fundamental mode is due to the anharmonicity of the Lennard-Jones potential near the minimum and not due to the cutoff at $r_c = 2.5\sigma_{ij}$.[50] To test this, we also carried out studies of anharmonic spring networks with $r_c \to \infty$ and found similar results.

In Fig. 3, we show that there is a qualitative change in the vibrational response when K increases from 5×10^{-6} to 5×10^{-5}. At the higher value of K, the vibrational response is noisy and energy is redistributed over a much wider range of frequencies than at the lower value of K. A more refined search shows that this qualitative change occurs in the kinetic energy interval $5 \times 10^{-5.50} < K_r < 5 \times 10^{-5.49}$, as shown in Fig. 4(a).

We now investigate the cause for the qualitative change in the vibrational response for $K > K_r$. To do this, for each fluctuating configuration $\mathbf{R}(t)$, we calculate the corresponding inherent structure or the configuration of the nearest local potential minimum $\mathbf{R}_0(t)$, using conjugate gradient energy minimization. A schematic illustrating the potential energy landscape is shown in Fig. 4(b). In Fig. 4(c), we plot the difference in the potential energy per atom $\Delta U(\mathbf{R}_0(t), \mathbf{R}_0(0)) = U(\mathbf{R}_0(t)) - U(\mathbf{R}_0(0))$ as a function of time for

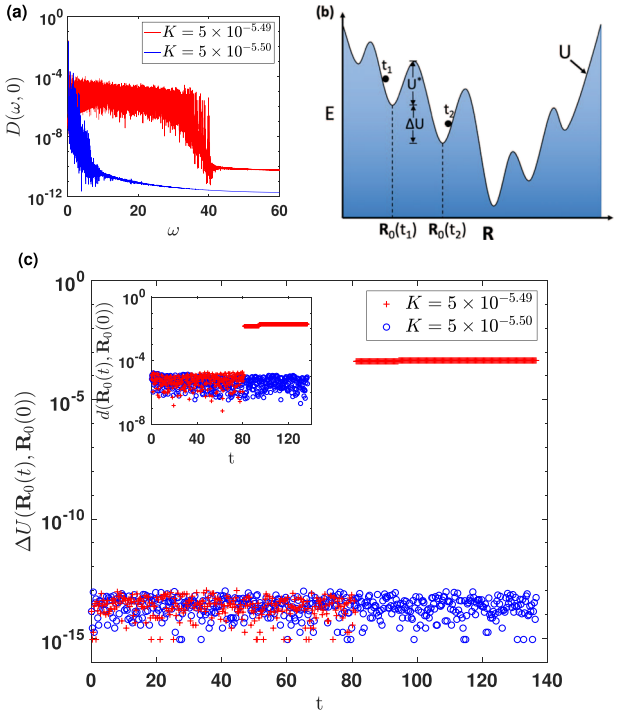

FIG. 4. (a) Power spectrum of the kinetic energy $D(\omega, 0)$ (during the first time interval $t = 0$) for $K = 5 \times 10^{-5.50}$ (blue) and $5 \times 10^{-5.49}$ (red). (b) Schematic diagram of the energy landscape with axes, the total energy per atom $E = U + K$, and atomic configuration $\mathbf{R}$. The configurations $\mathbf{R}_0(t_1)$ and $\mathbf{R}_0(t_2)$ represent the inherent structures (i.e., the nearest local potential energy minima) of the vibrating system at times t_1 and t_2, respectively. ΔU is the difference in the potential energy per atom, and U^* is the energy barrier between the configurations $\mathbf{R}_0(t_1)$ and $\mathbf{R}_0(t_2)$. (c) $\Delta U(\mathbf{R}_0(t), \mathbf{R}_0(0))$ between the inherent structures at times t and 0 for $K = 5 \times 10^{-5.50}$ (blue circles) and $5 \times 10^{-5.49}$ (red pluses). The inset shows the root-mean-square deviation (RMSD) $d(\mathbf{R}_0(t), \mathbf{R}_0(0))$ between the inherent structures at times t and 0.

$K < K_r$ and $K > K_r$. When $K < K_r$, $\Delta U \sim 10^{-14}$ for all times, indicating that the system remains in the basin of the inherent structure at $t = 0$. For $K > K_r$, ΔU jumps from $\sim 10^{-14}$ to $\sim 10^{-3}$ near $t^* \sim 80$, indicating that the system transitions from the basin of the inherent structure at $t = 0$ to that of a different inherent structure at t^* following an atomic rearrangement. We also used Eq. (4) to calculate the root-mean-square deviation between the inherent structures $\mathbf{R}_0(0)$ and $\mathbf{R}_0(t)$ at times 0 and t during the vibrations. In the inset of Fig. 4(c), we show that ΔU and d display similar behavior. For $K < K_r$, $d \sim 10^{-6}$ for all times. For $K > K_r$, near $t^* \sim 80$, d jumps from $\sim 10^{-6}$ to $\sim 10^{-2}$, again indicating that an atomic rearrangement occurs at t^*. One can also see that subsequent rearrangements occur at later times, which are indicated by jumps in ΔU and d. These results emphasize that atomic rearrangements induce significant redistribution of energy from the fundamental mode to other frequencies.

We quantify the leakage of energy from the fundamental mode to other frequencies over the first time interval $t = 0$ by calculating the loss $L(0)$ [defined in Eq. (2)] as a function of K in Fig. 5. We calibrate the measurement of the loss by studying perfect cosine

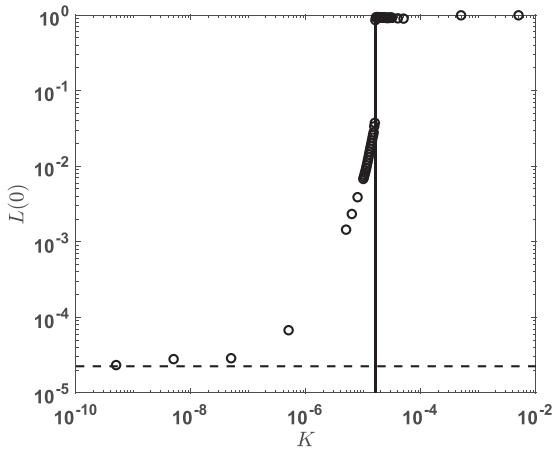

FIG. 5. Loss $L(0)$ [Eq. (2)] for the first time interval $t = 0$ vs the initial kinetic energy per atom K. The solid vertical line indicates $K_r \approx 5 \times 10^{-5.49}$ at which the first atomic rearrangement occurs. The dashed horizontal line indicates the loss threshold L_l for a harmonic oscillator with a measurement time δt that deviates from an integer.

oscillations of the velocity of a single atom over a tape length of δt. Since in general δt is not an exact integer multiple of the oscillation period, the loss $L_l \sim 10^{-4.5}$ we measured for a cosine wave is small but nonzero. We find that the lower threshold for the loss L_l does not affect the results we present. In Fig. 5, we show that at small K, $L(0) \sim L_l$ and $L(0)$ increases smoothly with increasing K until reaching 0.04 near K_r. At K_r, the loss jumps to $L(0) \sim 1$, indicating the onset of atomic rearrangements, and remains there for $K > K_r$.

In Fig. 5, we showed the loss for only the first time interval $t = 0$. We characterize the time-dependent loss in Fig. 6(a). [We also include the variation of the power spectrum of the kinetic energy $D(\omega, t)$ with time t in Appendix C.] We identify three distinct regimes. First, when $K < K_{nl}$, with $K_{nl} \approx 1.15 \times 10^{-5}$, the loss $L(t)$ is small and does not increase with t, and thus, $Q \to \infty$ over the time period we consider. In the second regime, for intermediate $K_{nl} < K < K_r$ [such as $K = 1.20 \times 10^{-5}$ in Fig. 6(a)], $L(t)$ initially increases with t smoothly, generating a finite Q, but then, $L(t)$ reaches a plateau and $Q \to \infty$ at the longest times we consider. In the third regime, for $K > K_r$ [such as $K = 1.26 \times 10^{-5}$ in Fig. 6(a)], $L(t)$ increases with t smoothly (indicating finite Q), until an atomic rearrangement event occurs and $L(t)$ jumps to a large value $L \sim 1$. $L(t)$ continues to increase after the first atomic rearrangement.

We evaluate $Q(0)$ for the first time interval $t = 0$ using Eq. (3) and show the results as a function of K in Fig. 6(b). We find that $Q(0) \sim 2 \times 10^4$ for $K \sim 1.5 \times 10^{-5}$ and $Q(0)$ increases with decreasing K. For $K \lesssim K_r$, Q begins to increase sharply, diverging as $K \to K_{nl}$, indicating the behavior for a perfect harmonic resonator for $K < K_{nl}$. We also find that $Q(0)$ vs $K - K_r$ is similar for samples with different initial configurations. These results indicate that to design a high-Q metallic glass resonator, one needs to fabricate a system with a large value for K_r and operate the resonator at $K < K_r$.

To understand the nature of oscillations in metallic glass resonators [e.g., $U(t)$ in Figs. 7(a) and 7(c)], we calculate the point

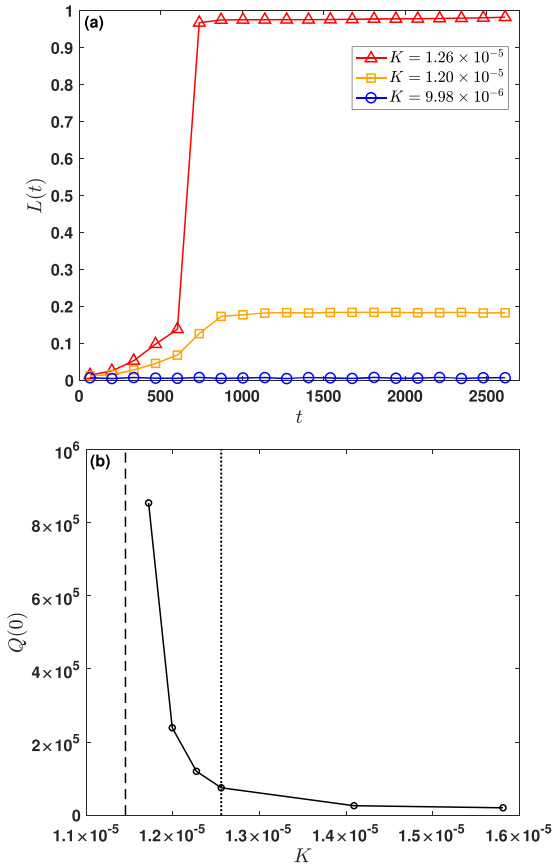

FIG. 6. (a) Loss $L(t)$ vs the time interval t for kinetic energy per atom $K = 9.98 \times 10^{-6}$ (blue circles), 1.20×10^{-5} (orange squares), and 1.26×10^{-5} (red triangles). (b) Quality factor $Q(0)$ for the first time interval $t = 0$ as a function of K. The dashed vertical line indicates $K_{nl} \approx 1.15 \times 10^{-5}$ at which $Q(0) \to \infty$ over the time period we consider. The vertical dotted line indicates $K_r \approx 1.26 \times 10^{-5}$, above which atomic rearrangements occur.

RMSD $d_{\text{point}}(t)$ and path RMSD $d_{\text{path}}(t)$ in Figs. 7(b) and 7(d). $d_{\text{point}}(t)$ quantifies the deviations in the configurations that are the closest to the potential energy minimum in each half cycle, and $d_{\text{path}}(t)$ quantifies the deviations in the configurations at corresponding times before and after the turning point of the oscillation during each half cycle.

When $K < K_{nl}$ (regime 1), the system is in the harmonic response regime, the path in configuration space followed by the resonator is nearly parabolic, as shown in Fig. 7(e), and both d_{point} and $d_{\text{path}} \sim 0$. When the system enters the anharmonic regime, $K_{nl} < K < K_r$ (regime 2), d_{point} and d_{path} [as well as the loss $L(t)$ in Fig. 6(a)] increase with t until $t^* \approx 790$. For $t > t^*$, d_{point}, d_{path}, and $L(t)$ reach plateaus and then remain nearly constant in time. This behavior indicates that the resonator is undergoing *anharmonic* oscillations, in which the system does not retrace the same configurations above and below the turning point for each half cycle, but the system is nearly reversible [see Fig. 7(f)]. In the third regime $K > K_r$, the probability for an atomic rearrangement increases strongly. In this regime, the system can traverse the saddle points,

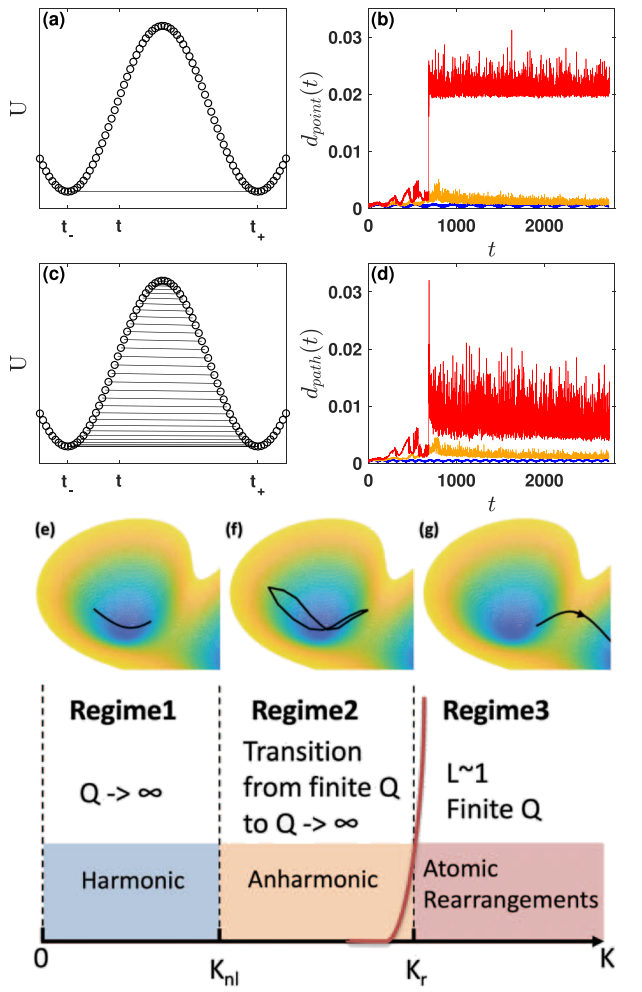

FIG. 7. (a) and (c) Total potential energy per atom U as a function of time from 0 to $n\delta t$, where $n = 20$. The times t_- and t_+ indicate successive times at which U is at a minimum during each half cycle of the vibrations. The horizontal solid line in (a), connecting the times t_- and t_+, indicates the times for each half cycle at which the RMSD, $d_{\text{point}}(\mathbf{R}(t_-), \mathbf{R}(t_+))$, is calculated in panel (b). In (b), we show d_{point} for $K = 9.98 \times 10^{-6}$ in the regime $K < K_{nl}$ (blue), $K = 1.20 \times 10^{-5}$ in the regime $K_{nl} < K < K_r$ (orange), and $K = 1.26 \times 10^{-5}$ in the regime $K > K_r$ (red). The horizontal solid lines in (c) indicate the times t_i and $t_j = t_+ + t_- - t_i$ during each half cycle that are used to calculate the RMSD, $d_{\text{path}} = \langle d(\mathbf{R}(t_i), \mathbf{R}(t_j))\rangle_{t_i}$, where the angle brackets indicate an average over the $1/2\Delta t \sim 300$ uniformly spaced times t_i. d_{path} in panel (d) is shown for the same values of K as in (b). (e)–(g) Schematic diagram that shows the system trajectories (solid black lines) in the potential energy landscape [shaded contours from high (orange) to low (blue) energies] for the three regimes of oscillations (1: $K < K_{nl}$, 2: $K_{nl} < K < K_r$, and 3: $K > K_r$). The red solid line indicates the probability of an atomic rearrangement vs K.

can enter the basins corresponding to new potential energy minima, and is thus microscopically irreversible. The three regimes describing resonator oscillations are summarized in Figs. 7(e)–7(g). Note that it is possible that the quality factor Q in regimes 1 and 2 is not strictly infinite but instead just extremely large and possibly time-dependent.[36] This issue will be discussed further in Appendix D.

B. Methods to increase K_r and enhance Q

In Sec. III A, we showed that even single atomic rearrangements give rise to significant loss and finite values of Q. Thus, to generate high-Q resonators, one must maximize $\langle K_r\rangle \sim \langle U^*\rangle$, yielding systems with large potential energy barriers. In this section, we describe studies of the ensemble-averaged $\langle K_r\rangle$ vs system size N and cooling rate R, averaged over typically 20 independently generated initial conditions. For each R and N, we excite the resonator along the fundamental mode corresponding to the lowest eigenvalue of the dynamical matrix ω_1 and monitor the system during the first time interval $t = 0$ as a function of K.

In Fig. 8(a), we show that the ensemble-averaged kinetic energy per atom at which the first atomic rearrangement occurs, $\langle K_r\rangle$, decreases with increasing N. We find that $\langle K_r\rangle \sim N^{-2k}$, where $k \approx 0.68$ for $R = 10^{-2}$ and ≈ 0.60 for $R = 10^{-5}$. $\langle K_r\rangle$ is smaller for rapidly compared to slowly cooled glasses since $\langle U^*\rangle$ decreases with increasing R.[23,51,52] These results emphasize that Q can be increased by making resonators smaller and preparing them using slower cooling rates. For example, experimental studies of Pt-based metallic glass microcantilevers have reported that the quality factor can be increased by more than a factor of 3 after annealing.[9]

Using a typical energy scale of 0.1 eV for the depth of the pair potential for NiP metallic glasses,[53] we find that the characteristic temperature scale associated with K_r for a Lennard-Jones system with $N = 8000$ atoms is on the order of several millikelvin. Thus, our results are most relevant to those for low-temperature experiments, where the transfer of energy out of a single eigenmode can be monitored, and not to room temperature experiments, where atomic rearrangements occur frequently and equipartition can be achieved. For example, there have been low-temperature experiments focused on the vibrational properties of amorphous silica,[54,55] polycrystalline aluminum,[56] and other crystalline and amorphous solids. All of these experimental studies considered temperatures between 0.1 mK and 1 K.

We can also compare the kinetic energy per atom $\langle K_r\rangle$ required to induce the first atomic rearrangement in thermally vibrating systems to the characteristic shear strain $\langle \gamma_r\rangle$ required to induce the first atomic rearrangement in systems driven by athermal quasistatic (AQS) shear. To calculate $\langle \gamma_r\rangle$, we confine N atoms interacting via the Kob-Andersen model to cubic boxes with periodic boundary conditions in the x-, y-, and z-directions. We cool the samples from temperature T_0 to zero using a linear ramp over a range of cooling rates R from 10^{-5} to 10^{-2}. For each sample, we perform AQS pure shear at fixed volume V, i.e., at each strain step, we expand the box length and move all atoms affinely in the x-direction by a small strain increment $\delta\gamma_x = \delta\gamma = 10^{-4}$ and compress the box length and move all atoms affinely in the y-direction by the same strain increment $\delta\gamma_y = -\delta\gamma$. Following each strain step, we perform conjugate gradient energy minimization at fixed volume. To measure $\langle \gamma_r\rangle$, we employ the method we developed previously[21] to unambiguously determine whether an atomic rearrangement occurs with an accuracy on the order of numerical precision. As shown in Fig. 8(c), we find that $\langle \gamma_r\rangle \sim N^{-\kappa}$ also decreases with increasing N, where the system-size

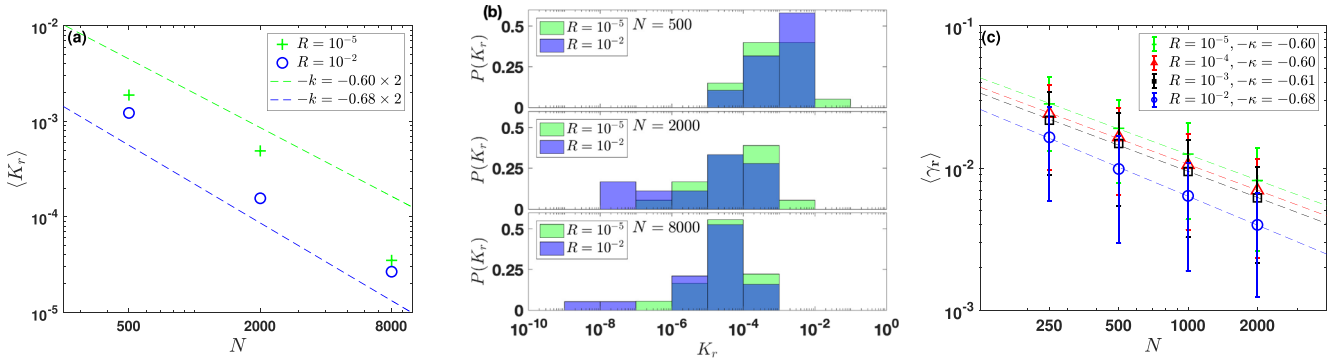

FIG. 8. (a) The ensemble-averaged kinetic energy per atom $\langle K_r \rangle$ above which the first atomic rearrangement occurs vs system size N for rapidly and slowly cooled glasses with $R = 10^{-2}$ (blue circles) and 10^{-5} (green pluses), respectively. In each case, $\langle K_r \rangle$ is averaged over 20 independent samples. The slopes of the dashed lines are $-k$. (b) Probability distribution $P(K_r)$ for the samples in (a), prepared with cooling rates $R = 10^{-2}$ and $R = 10^{-5}$ and system sizes $N = 500$, 2000, and 8000. (c) Ensemble-averaged pure shear strain $\langle \gamma_r \rangle$ above which the first atomic rearrangement occurs during athermal, quasistatic pure shear vs system size N for glasses prepared using $R = 10^{-2}$ (blue circles), 10^{-3} (black squares), 10^{-4} (red triangles), and 10^{-5} (green pluses). $\langle \gamma_r \rangle$ is averaged over 500 samples, and the error bars represent the standard deviations. The negative κ-values give the slopes of the dashed lines.

scaling exponent $\kappa \sim 0.6$–0.68 is again only weakly dependent on the cooling rate. These results for the system-size scaling exponents in athermal quasistatic shear are consistent with dimensional arguments that suggest $\kappa \sim 2k$, and thus, athermal quasistatic shear can be used to understand the low temperature properties of glasses.

Using these results, we can estimate the strains below which resonators can operate in the harmonic response regime. For the slowest cooling rate $R = 10^{-5}$, we find that $\log_{10}\langle \gamma_r \rangle \approx -2k \log_{10} N + \gamma_\infty$, where $2k \approx 0.60$, $\gamma_\infty \approx 0.11$, $N = \rho(l/D)^3$, the number density $\rho \approx 1.2$, $D \approx 3.7$ Å is a typical atomic diameter for $Ni_{80}P_{20}$ metallic glasses[53] (which is the subject of the Kob-Andersen model), and l is a characteristic lengthscale of the resonator. We find that $\langle \gamma_r \rangle \sim 5 \times 10^{-4}$ for a resonator with $l \sim 20$ nm, whereas $\langle \gamma_r \rangle \sim 3 \times 10^{-8}$ for a resonator with $l \sim 5$ μm.[57,58] Micrometer-scale metallic glass resonators have been fabricated as hemispherical shells[10] and as cantilevers.[9] In addition, strains in the range from 10^{-7} to 10^{-4} have been used in measurements of internal friction in metallic glass resonators.[59] Our results emphasize that nano-sized metallic glass resonators operating in the small strain (e.g., $<10^{-7}$) and low temperature regimes are promising high-Q materials.

There have been a number of experimental studies[60–62] that have shown that metallic glasses at room temperature are stronger and more dissipative in smaller samples compared to larger ones. In contrast, here we show that our model resonators composed of atoms with Lennard-Jones-like interactions show less loss as the system size decreases since K_r decreases with increasing system size N. A key difference between our computational studies and the experimental studies is that ours are carried out at extremely low temperature and applied strains, while the above-mentioned experiments were carried out at room temperature and finite strains. An important aspect of our work is that we show that atomic rearrangements can cause significant loss even at such low temperatures and strains.

C. Comparison between crystalline and amorphous resonators

In Sec. III B, we showed that the characteristic kinetic energy per atom $\langle K_r \rangle$ above which atomic rearrangements occur increases modestly with decreasing cooling rate. Furthermore, we know that crystalline ordering increases with decreasing cooling rate. Does this imply that crystalline metals are higher-Q materials compared to amorphous metals? In this section, we calculate $\langle K_r \rangle$ for resonators made from single crystal, polycrystalline, and defected crystalline materials and compare these results to those for resonators made from homogeneously amorphous samples.

Crystalline metals often contain slip planes, dislocations, grain boundaries, and other defects, and the defect density typically increases with increasing cooling rate. To generate crystalline materials with defects in simulations, we will again use the Kob-Andersen model, but with monodisperse atoms, $\varepsilon_{AA} = \varepsilon_{AB} = \varepsilon_{BB} = 1.0$ and $\sigma_{AA} = \sigma_{AB} = \sigma_{BB} = 1.0$, to enhance crystallization. We will employ the same protocol as discussed in Sec. II to generate thin-bar resonators with $N = 2000$ and aspect ratio L_x:L_y:L_z = 6:1:2 over a range of cooling rates from $R = 10^{-4}$ to 10^{2}. The method of excitation and measurement of the loss and K_r are also the same as described in Sec. II.

Snapshots of the zero-temperature thin-bar resonators generated using six different cooling rates are shown in Fig. 9 (with periodic boundary conditions and prior to adding excitations). We use the Common Neighbor Analysis (CNA)[63] to identify atoms that occur in crystalline [either face-centered cubic (fcc) or hexagonal close packed (hcp)] and amorphous environments in the thin bars. In Fig. 10(a), we show that the ensemble-averaged fraction of crystalline atoms $\langle f_X \rangle$ decreases with increasing R. $\langle f_X \rangle$ is nearly 90% when $R = 1.2 \times 10^{-4}$ and $\langle f_X \rangle = 0$ for $R = 1.2 \times 10^{-1}$. Near the critical cooling rate $R_c \approx 10^{-2.5}$, the system contains a roughly equal mixture of atoms in crystalline and amorphous environments.

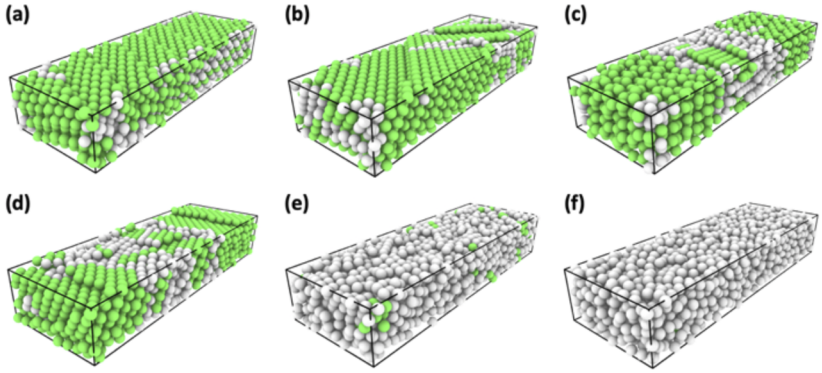

FIG. 9. Snapshots of thin-bar-shaped resonators with $N = 2000$ monodisperse atoms obtained using cooling rates (a) $R = 1.2 \times 10^{-4}$, (b) 1.2×10^{-3}, (c) 3×10^{-3}, (d) 6×10^{-3}, (e) 1.2×10^{-2}, and (f) 1.2×10^{-1} in periodic boundary conditions prior to applying the excitations. Atoms with crystalline (fcc or hcp) order are colored green, while amorphous atoms are colored gray.

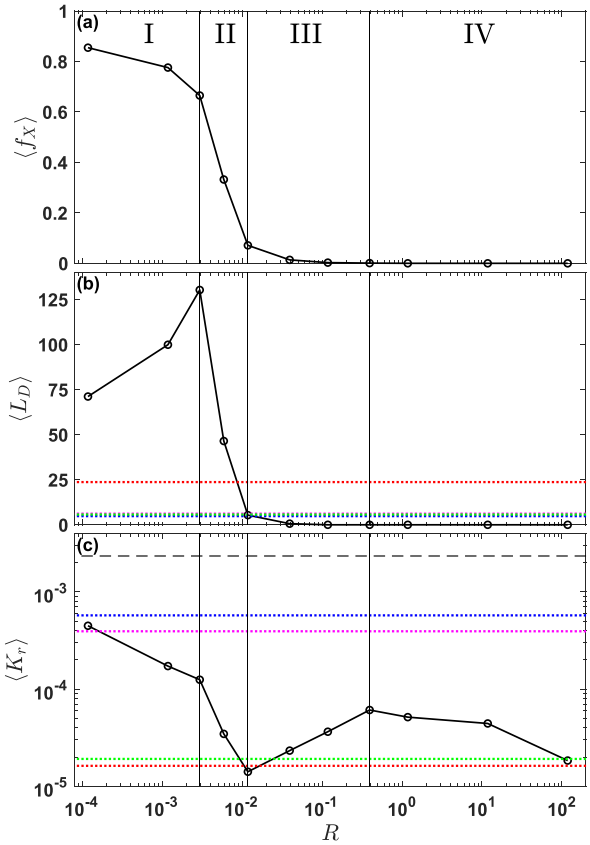

FIG. 10. (a) Fraction of crystalline atoms $\langle f_X \rangle$, (b) total dislocation length $\langle L_D \rangle$, and (c) kinetic energy per atom $\langle K_r \rangle$ above which atomic rearrangements occur as a function of cooling rate R for resonators made using the monodisperse Kob-Andersen model. The ensemble averages are obtained by averaging over at least 10 independent samples. The dotted horizontal lines in (b) and (c) show $\langle L_D \rangle$ and $\langle K_r \rangle$ for four nearly perfect, crystalline thin bars with specifically placed defects. For example, the red dotted lines represent the thin-bar sample in Fig. 11. The black dashed line in (c) shows $\langle K_r \rangle$ for a thin bar with perfect fcc order. The solid vertical lines in panels (a)–(c) give approximate boundaries between the four regimes of vibrational response as a function of cooling rate R.

To quantify disorder in the thin-bar samples, we used the Dislocation Extraction Analysis (DXA) tool within the OVITO software library.[64] DXA allows us to measure the total dislocation length L_D, which gives the sum of the magnitudes of the Burgers vectors for each dislocation in the sample. For $R \ll 1$, we expect few defects, and thus, $\langle L_D \rangle \to 0$. In Fig. 10(b), for small R, we show that L_D increases with cooling rate R.[7,27] When $R > 3 \times 10^{-3}$, $\langle L_D \rangle$ drops sharply since the thin-bar samples include mixtures of atoms with crystalline and amorphous environments. $L_D \to 0$ when the sample becomes completely amorphous.

To determine the vibrational response, we excite the fundamental mode ω_1 for each sample and measure $\langle K_r \rangle$ as a function of R. The behavior for $\langle K_r \rangle$ can be divided into four regimes [see Fig. 10(c)]. First, at low cooling rates $R \lesssim 3 \times 10^{-3}$ (regime I), the systems are mostly crystalline with sparse dislocations. In this regime, as R increases, more dislocations are formed and $\langle L_D \rangle$ increases, which causes $\langle K_r \rangle$ to decrease. In regime II, at intermediate cooling rates $3 \times 10^{-3} \lesssim R \lesssim 1.2 \times 10^{-2}$, $\langle f_X \rangle$ drops sharply and the thin bars contain mixtures of crystalline and amorphous atoms. The additional boundaries between amorphous and crystalline regions of the system cause a larger decrease in $\langle K_r \rangle$ than at smaller R. In regime III, $1.2 \times 10^{-2} \lesssim R \lesssim 3 \times 10^{-1}$, the thin-bar resonators become homogeneously amorphous and metastable, causing $\langle K_r \rangle$ to increase by a factor of ≈ 4. At the high cooling rates $R \gtrsim 3 \times 10^{-1}$ in regime IV, $\langle K_r \rangle$ will decrease modestly with increasing R. For the Kob-Andersen bidisperse mixture, we have already shown in Fig. 8(a) that $\langle K_r \rangle$ decreases by a factor of ≈ 3 as R is increased over three orders of magnitude. This local maximum in $\langle K_r \rangle(R)$ is interesting because it shows that there is a regime where amorphous resonators can have larger Q-values than partially crystalline resonators.

In addition to studying the vibrational response of thin-bar resonators generated by cooling a high-temperature liquid into a solid, we also investigated the vibrational response of systems for which we started with perfect fcc crystalline thin bars and generated specifically placed defects. In particular, we generated four thin-bar samples that were initialized with perfect fcc order, and then, we removed a slot with a width of one atom, depth of two atoms, and varying lengths along different directions in the sample. An example is shown in Fig. 11. We display $\langle L_D \rangle$ and $\langle K_r \rangle$ for these four

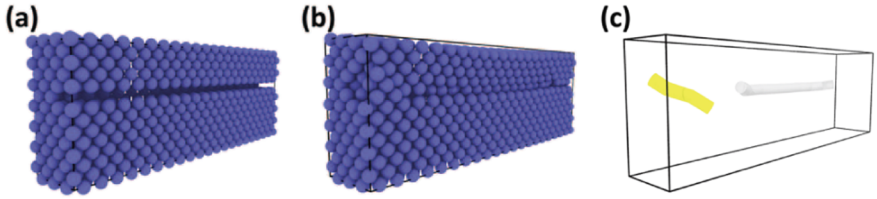

FIG. 11. Snapshots of thin-bar crystalline resonators with a specifically placed defect. In (a), we delete a row of atoms from a resonator with perfect fcc order and perform energy minimization, which yields the thin-bar resonator in (b). (c) We identify two dislocations in the resonator in (b) colored yellow and gray.

systems in Figs. 10(b) and 10(c). These samples possess a range of $\langle K_r \rangle$: some values are larger than that of the rapidly cooled glass ($R = 1.2 \times 10^{-1}$), while others are not. These results show that amorphous resonators can possess values of $\langle K_r \rangle$ (and thus Q) that are comparable to those for crystalline samples. For example, the thin-bar resonator corresponding to the green dotted horizontal line in Fig. 10(c) possesses a smaller $\langle K_r \rangle$ than that of the rapidly cooled glass, with a dislocation density $\langle L_D \rangle / V \approx 2 \times 10^{16}$ m^{-2}, which is similar to values for crystalline metals with strong dislocations.[65] Since metallic glasses do not need to be annealed, can be molded into complex shapes, possess unique magnetic and biocompatibility properties,[15–17,66,67] and can possess comparable quality factors to crystalline metals,[9] metallic glasses are promising materials for high-Q applications.

IV. CONCLUSION

In this article, we employ molecular dynamics simulations of model metallic glass resonators undergoing vibrations to quantify the intrinsic dissipation and loss mechanisms caused by thermal fluctuations and atomic rearrangements. Using thin-bar resonators generated over a wide range of cooling rates, we excite the fundamental mode corresponding to the lowest eigenfrequency ω_1 of the dynamical matrix as a function of the kinetic energy per atom K. We find three regimes of vibration. In the harmonic response regime, $K < K_{nl}$, most of the energy of the vibrations remains in the fundamental mode, the loss is small, and $Q \to \infty$ over the time period we consider (since we do not consider coupling of the resonator to the environment). For $K_{nl} < K < K_r$, energy can leak from the fundamental mode to others at short times, but at sufficiently long times, the leakage of energy to other frequencies stops, and thus, $Q \to \infty$ at the longest times we consider. For $K > K_r$, one or more atomic rearrangements occur. In this regime, energy in the fundamental mode is completely redistributed to a large set of other frequencies, the loss is large, and Q is finite. Thus, we show that K_r strongly affects the quality factor.

We find that $\langle K_r \rangle$ decreases as a power-law N^{-k} with increasing system size N, where $k \approx 1.3$ decreases only modestly with decreasing R. We find similar results for the critical shear strain $\langle K_r \rangle \sim \langle \gamma_r \rangle^2$ using athermal quasistatic shear deformation, where $\langle \gamma_r \rangle$ is the characteristic strain above which atomic rearrangements begin to occur. Using these results, we estimate that $\langle \gamma_r \rangle \sim 10^{-8}$ for micrometer-sized resonators, and thus, large Q-values can be obtained when these resonators are operated at $\gamma < \langle \gamma_r \rangle$ at low temperatures. We also measured $\langle K_r \rangle$ in thin-bar resonators with crystalline order and compared the vibrational response to that in amorphous resonators. We find that $\langle K_r \rangle$ is similar for amorphous resonators and those with significant crystalline order. In light of the fact that metallic glasses can be thermoplastically formed into complex shapes, possess unique magnetic and biocompatibility properties, and can achieve Q-values that are comparable to those for crystalline structures (at low temperatures), metallic glasses are promising materials for micro- and nanoresonators.

Our results raise a number of interesting future directions. For example, we can investigate methods that involve mechanical deformation, not slower cooling rates or annealing methods, to increase $\langle K_r \rangle$ and move the sample to regions of configuration space with higher energy barriers between inherent structures. One possible approach is to apply athermal cyclic simple or pure shear deformation to samples that have been prepared using fast cooling rates. Recent studies have found that there is a finite critical strain amplitude for cyclic shear that marks the limit between reversible and irreversible atomic rearrangements in the large-system limit.[68–70] Does this imply that cyclic shear training can find zero-temperature configurations for which $\langle K_r \rangle$ remains finite in the large-system limit? In addition, we can explore how the type of cyclic driving affects $\langle K_r \rangle$ and whether configurations can be trained in multiple directions simultaneously to increase $\langle K_r \rangle$. Another future direction involves studies of the loss and quality factor when the resonator has clamped instead of free boundary conditions and when it is driven over a range of frequencies, not only the fundamental mode. It is also important to compare the results of our studies that consider systems at constant energy to the vibrational response of systems sheared at finite strain rate and coupled to a thermostat.[71]

ACKNOWLEDGMENTS

The authors acknowledge support from NSF MRSEC, Grant No. DMR-1119826 (M.F. and C.S.O.), and NSF, Grant Nos. CMMI-1462439 (M.F. and C.S.O.) and CMMI-1463455 (M.S.). This work was supported by the High Performance Computing facilities operated by, and the staff of, the Yale Center for Research Computing.

APPENDIX A: LOW-FREQUENCY EIGENMODES OF THE RESONATOR

In the main text, we focused on samples with $N = 2000$ atoms, rectangular cross section, and aspect ratios, $L_x/L_y = 6$ and $L_z/L_y = 2$. The elongated, asymmetric shape of the samples was selected so that the lowest eigenfrequency is well-separated from other low-frequency modes. Having well-separated low-frequency

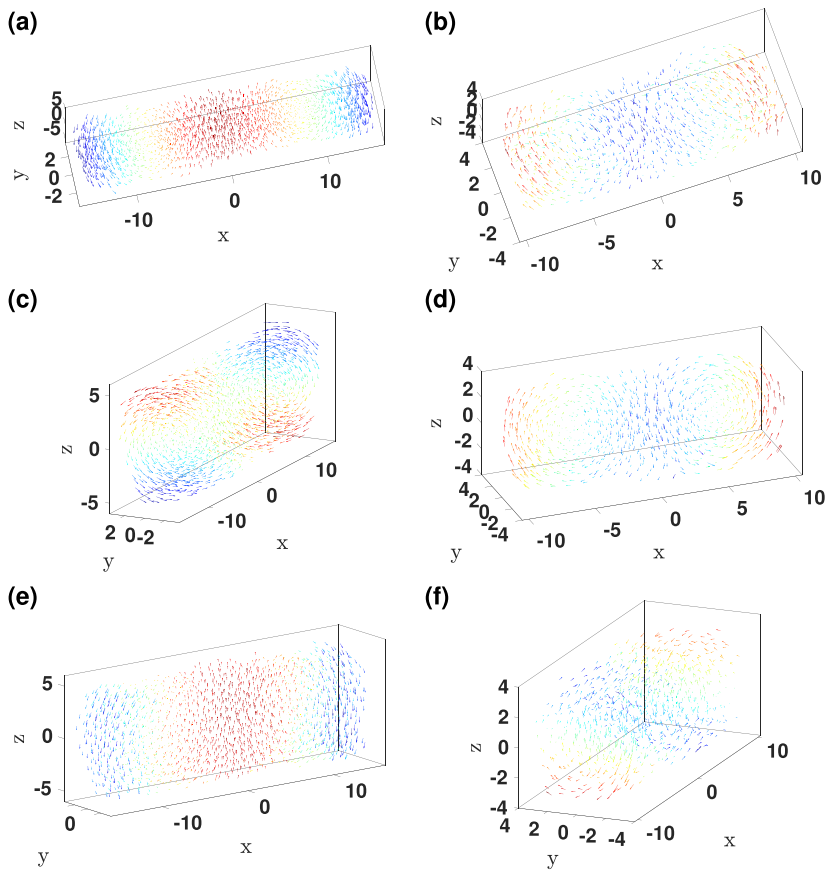

FIG. 12. Vector fields representing the first three eigenmodes of the dynamical matrix for metallic glass samples with $N = 2000$ and aspect ratios $L_x/L_y = 6$ and $L_z/L_y = 2$ [(a), (c), and (e)] and $N = 1000$ and aspect ratios $L_x/L_y = 3$ and $L_z/L_y = 1$ [(b), (d), and (f)]. The color scale highlights the y- or z-component of the fundamental mode contribution for each atom with red corresponding to positive and blue corresponding to negative values.

modes makes it easier to study leakage of energy from the fundamental mode to other frequencies. For example, in Fig. 3, we analyzed the dynamical matrix for the $L_x/L_y = 6$ and $L_z/L_y = 2$ sample and found that the lowest three nontrivial eigenfrequencies are $\omega_1 = 0.171$, $\omega_2 = 0.270$, and $\omega_3 = 0.300$ [dashed vertical lines in Fig. 3(b)]. We display the eigenmodes corresponding to these three eigenfrequencies in Fig. 12. ω_1 and ω_3 correspond to bending modes, and ω_2 corresponds to a torsional mode. To determine the effects of aspect ratio on the eigenmodes, we also calculated the eigenfrequencies and eigenmodes of the dynamical matrix for a more symmetric bar with $N = 1000$ atoms and aspect ratios $L_x/L_y = 3$ and $L_z/L_y = 1$. The results are summarized in Table I and Fig. 12. ω_1 and ω_2 correspond to bending modes, and ω_3 corresponds to a torsional mode. The lowest eigenfrequency ω_1 of the bar with $L_x/L_y = 6$ and $L_z/L_y = 2$ is much smaller than ω_2 and ω_3, and $\omega_1 \sim \omega_2 \sim \omega_3$ for a bar with $L_x/L_y = 3$ and $L_z/L_y = 1$.

TABLE I. The aspect ratios and system sizes of the metallic glass thin-bar resonators considered in the computational studies of the quality factor. We show the lowest three eigenfrequencies of the dynamical matrix for these systems and describe their spatial structure. Visualizations of the eigenmodes are shown in Fig. 12.

Aspect ratios L_x/L_y and L_z/L_y and system size N	(Lowest three) eigenfrequencies	Panel number of Fig. 12 that shows corresponding eigenmode	Mode structure	Color scale
$L_x/L_y = 6$, $L_z/L_y = 2$, $N = 2000$	$\omega_1 = 0.17$	(a)	Bending in xy-plane	y-component
	$\omega_2 = 0.27$	(c)	Torsion	y-component
	$\omega_3 = 0.30$	(e)	Bending in xz-plane	z-component
$L_x/L_y = 3$, $L_z/L_y = 1$, $N = 1000$	$\omega_1 = 0.42$	(b)	Bending in xy-plane	y-component
	$\omega_2 = 0.46$	(d)	Bending in xz-plane	z-component
	$\omega_3 = 0.51$	(f)	Torsion	y-component

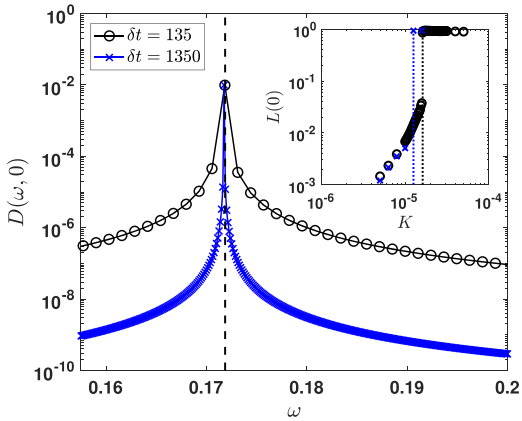

FIG. 13. The low-frequency regime for the power spectrum of the kinetic energy (for the first time interval $t = 0$) $D(\omega, 0)$ near the fundamental frequency $\omega_1 \approx 0.172$ (vertical dashed line) calculated using time series with two different total lengths, $\delta t = 135$ (black circles) and 1350 (blue exes), at $K = 5 \times 10^{-6}$ in the harmonic response regime. In the inset, we show the loss $L(0)$ vs K for the same time series in the main panel. The characteristic kinetic energy per atom above which an atomic rearrangement occurs is indicated: $K_r = 1.62 \times 10^{-6}$ (black dotted line) for $\delta t = 135$ and $K_r = 1.26 \times 10^{-6}$ (blue dotted line) for $\delta t = 1350$.

APPENDIX B: DEPENDENCE ON THE LENGTH OF THE TIME SERIES

In the main text, we used a total run length of $\delta t = 135$ to calculate the power spectrum of the kinetic energy and loss for the first time interval $t = 0$ in Figs. 3 and 5 (as well as all other time intervals). In this appendix, we show results for $D(\omega, 0)$ when δt is increased by a factor of 10 (keeping the sampling rate fixed). In Fig. 13, for $K < K_r$ in the harmonic response regime, we show that the peak value of $D(\omega_1, 0)$ is unchanged for $\delta t = 135$ and 1350, and thus, $L(0)$ is nearly the same for the two values of δt. We know that the probability for an atomic rearrangement increases with time δt at fixed K. Thus, in the inset to Fig. 13, we show that the loss $L(0)$ undergoes a discontinuous jump for $\delta t = 1350$ at a smaller K than that for $\delta t = 135$. We find that $K_r \approx 1.62 \times 10^{-5}$ for $\delta t = 135$ and $\approx 1.26 \times 10^{-5}$ for $\delta t = 1350$. Thus, the precise value of K_r depends on δt, but all of the results are qualitatively the same for different choices of δt.

APPENDIX C: TIME-DEPENDENT POWER SPECTRUM OF THE KINETIC ENERGY

For the calculations of the power spectrum of the kinetic energy and loss in the main text, we divided a long time series following the excitation of the resonator along the fundamental mode into 20 time intervals of equal length δt. We showed the power spectrum of the kinetic energy $D(\omega, 0)$ for the first time interval (i.e., considering times from 0 to δt) in Fig. 3. In this appendix, we calculate $D(\omega, t)$ for all 20 time intervals. In Fig. 14, we show $D(\omega, t)$ for K values in the three regimes, $K < K_{nl}$, $K_{nl} < K < K_r$, and $K > K_r$, which match those used in Fig. 6(a). For $K < K_{nl}$, there is minimal leakage of energy from the fundamental mode $\omega_1 = 0.172$ and $Q \to \infty$ for the time period we consider. In the regime $K_{nl} < K < K_r$, energy leaks from the fundamental mode at short times, but it stops for $t/\delta t \gtrsim 12$, and the system vibrates anharmonically with finite loss, finite Q for $t/\delta t \lesssim 12$ and $Q \to \infty$ for $t/\delta t \gtrsim 12$. For $K > K_r$, strong energy leakage occurs due to an atomic rearrangement at $t/\delta t \approx 5$.

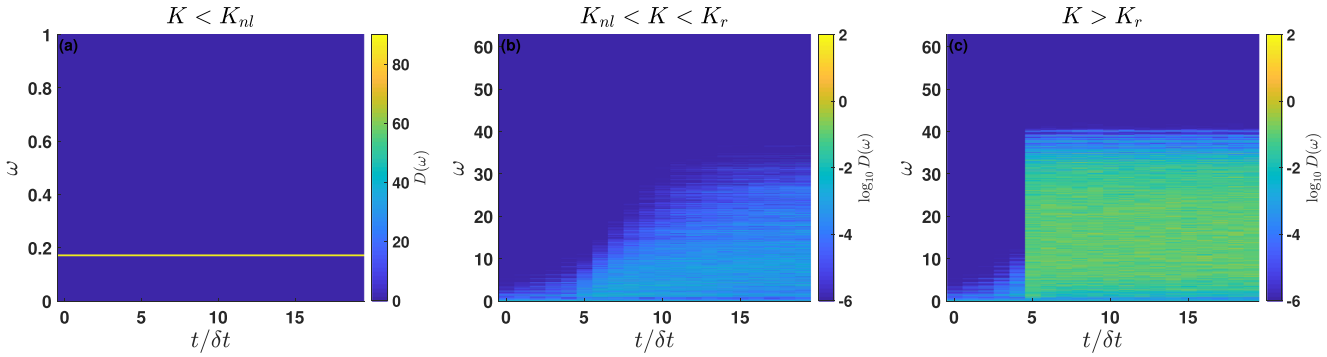

FIG. 14. The power spectrum of the kinetic energy at time t $D(\omega, t)$ vs time $t/\delta t$ in the three regimes for the kinetic energy per atom: (a) $K < K_{nl}$, (b) $K_{nl} < K < K_r$, and (c) $K > K_r$, for a $N = 2000$ thin-bar resonator with amorphous structure. The color scale from yellow to dark blue give decreasing values of $D(\omega, t)$ in panel (a), and $\log_{10} D(\omega, t)$ in panels (b) and (c).

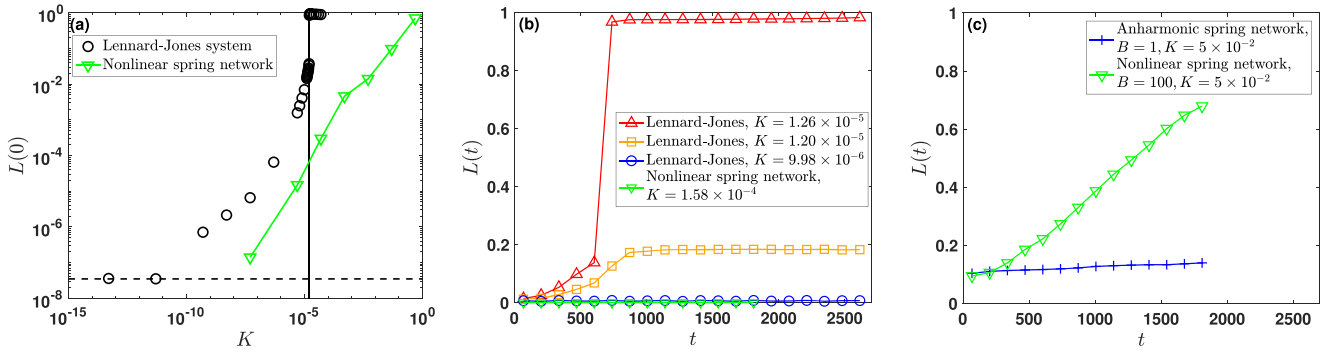

FIG. 15. (a) Loss $L(0)$ for the first time interval $t = 0$ vs the initial kinetic energy per atom K for a thin-bar resonator with atoms interacting via Lennard-Jones interactions vs nonlinear spring networks with $B = 100$. The solid vertical line indicates $K_r \approx 5 \times 10^{-5.49}$ at which the first atomic rearrangement occurs in the Lennard-Jones system. The dashed horizontal line indicates the loss threshold L_l for a harmonic oscillator with a dimensionless measurement time δt that deviates from an integer. (b) Loss $L(t)$ vs the time interval t for thin-bar resonators composed of atoms that interact via Lennard-Jones interactions with kinetic energy per atom $K = 9.98 \times 10^{-6}$, 1.20×10^{-5}, and 1.26×10^{-5} vs nonlinear spring networks (with $B = 100$) at $K = 1.58 \times 10^{-4}$. (c) Loss $L(t)$ vs the time interval t for nonlinear spring networks for $K = 5 \times 10^{-2}$ and $B = 1$ and 100.

APPENDIX D: VIBRATIONAL RESPONSE OF NONLINEAR SPRING NETWORKS

As discussed in the main text, there is an important difference between studies of equipartition in nonlinear spring networks (that do not rearrange) and in collections of Lennard-Jones atoms that can undergo atomic rearrangements. To investigate this difference, we carried out additional simulations to compare results for the loss for a Lennard-Jones glassy configuration [with the pair potential $u(r_{ij})$ given in Sec. II] and the same configuration, but with pair interactions between atoms i and j of the form for a nonlinear spring network: $u_s(r_{ij}) = 0.5\,A(r_{ij0})(r_{ij} - r_{ij0})^2 + A(r_{ij0})B(r_{ij} - r_{ij0})^4$, where r_{ij0} is the separation between atoms i and j in the reference configuration, $A(r_{ij0})$ is the second derivative of the Lennard-Jones potential with respect to r_{ij} at $r_{ij} = r_{ij0}$, and B is the coefficient of the fourth order term in $u_s(r_{ij})$. Note that in the nonlinear spring system, $u_s(r_{ij})$ has infinite range and does not tend to zero in the large-separation limit. We also maintain the list of neighbors for each atom at all times, and thus, for atoms interacting via $u_s(r_{ij})$, the atoms do not rearrange. For the systems with $u_s(r_{ij})$, we calculate the dynamical matrix, excite the lowest eigenmode of the system, and measure the loss as a function of time. Previously, we performed similar studies for models of granular media.[72]

In Fig. 15(a), we show the loss $L(0)$ for the first time interval $t = 0$ vs the initial kinetic energy per atom K for both the Lennard-Jones system and nonlinear spring network. At small K, we find that $L(0)$ shows a similar increase with K for the Lennard-Jones system and nonlinear spring network. $L(0)$ increases continuously over the full range of K for the nonlinear spring network, but $L(0)$ for the Lennard-Jones system increases much more dramatically as K approaches K_r when the system undergoes an atomic rearrangement. Thus, the nonlinear spring network requires a much larger value of K to achieve the same value of the loss $L(0)$ compared to the Lennard-Jones system. For example, at $K = K_r$, $L(0)$ for the Lennard-Jones system and nonlinear spring network differ by more than four orders of magnitude. This result is important; it shows that atomic rearrangements (which are not typically included in studies of nonlinear spring networks) play an important role in determining the transfer of energy out of the excited mode.

In Fig. 15(b), we compare the loss $L(t)$ as a function of the time interval t for the Lennard-Jones system and nonlinear spring network at comparable values of K near 10^{-5}. In this range of K for the nonlinear spring system, $L(t) \sim 10^{-4}$ and it does not change significantly with time. However, over the same range of K and time interval, $L(t)$ for the Lennard-Jones system varies significantly as the system approaches and crosses a potential energy barrier associated with an atomic rearrangement. We find that for $K < K_{nl}$, $L(t)$ for the Lennard-Jones system is small and does not show any significant time dependence. For $K_{nl} < K < K_r$, $L(t)$ for the Lennard-Jones system increases to ~0.2 and then remains nearly constant over the time range that we considered. And then for $K > K_r$, $L(t)$ increases dramatically, reaching $L \sim 1$ after an atomic rearrangement. Again, $L(t)$ is extremely small at all times considered over this range of K for the nonlinear spring network.

In Fig. 15(c), we show the loss $L(t)$ for the nonlinear spring network at a much larger value of K, i.e., $K = 0.05$. In this regime, $L(t)$ increases with time, yielding a finite value of Q, which decreases with increasing B. It is possible that the quality factor Q in the regimes of the kinetic energy per particle, $K < K_{nl}$ and $K_{nl} < K < K_r$, is not strictly infinite, but instead just extremely large and possibly time dependent. Even though determining whether or not $Q \to \infty$ in these regimes is important, it is not the main point of the manuscript. Instead, the key aspect of the manuscript is determining the effects of atomic rearrangements on the quality factor of metallic glass resonators.

REFERENCES

[1] B. Arash, J.-W. Jiang, and T. Rabczuk, "A review on nanomechanical resonators and their applications in sensors and molecular transportation," Appl. Phys. Rev. **2**, 021301 (2015).
[2] E. I. Green, "The story of Q," Am. Sci. **43**, 584–594 (1955).

[3]M. E. Tobar, J. Krupka, J. G. Hartnett, E. N. Ivanov, and R. A. Woode, "High-Q sapphire-rutile frequency-temperature compensated microwave dielectric resonators," IEEE Trans. Ultrason. Ferroelectr. Freq. Control **45**, 830–836 (1998).
[4]A. K. Huttel, G. A. Steele, B. Witkamp, M. Poot, L. P. Kouwenhoven, and H. S. van der Zant, "Carbon nanotubes as ultrahigh quality factor mechanical resonators," Nano Lett. **9**, 2547–2552 (2009).
[5]H. Jiang, M.-F. Yu, B. Liu, and Y. Huang, "Intrinsic energy loss mechanisms in a cantilevered carbon nanotube beam oscillator," Phys. Rev. Lett. **93**, 185501 (2004).
[6]P. Ovartchaiyapong, L. Pascal, B. Myers, P. Lauria, and A. Bleszynski Jayich, "High quality factor single-crystal diamond mechanical resonators," Appl. Phys. Lett. **101**, 163505 (2012).
[7]M. S. Blanter, I. S. Golovin, H. Neuhauser, and H. Sinning, *Internal Friction in Metallic Materials* (Springer, 2007).
[8]V. Khonik and L. Spivak, "On the nature of low temperature internal friction peaks in metallic glasses," Acta Mater. **44**, 367–381 (1996).
[9]M. Kanik, P. Bordeenithikasem, G. Kumar, E. Kinser, and J. Schroers, "High quality factor metallic glass cantilevers with tunable mechanical properties," Appl. Phys. Lett. **105**, 131911 (2014).
[10]M. Kanik, P. Bordeenithikasem, D. Kim, N. Selden, A. Desai, R. M'Closkey, and J. Schroers, "Metallic glass hemispherical shell resonators," J. Microelectromech. Syst. **24**, 19–28 (2015).
[11]Y. Hiki, R. Tamura, and S. Takeuchi, "Internal friction of metallic glass measured as function of strain amplitude at various temperatures," Mater. Sci. Eng.: A **521**, 228–231 (2009).
[12]J. A. Bardt, G. R. Bourne, T. L. Schmitz, J. C. Ziegert, and W. G. Sawyer, "Micromolding three-dimensional amorphous metal structures," J. Mater. Res. **22**, 339–343 (2007).
[13]M. Ashby and A. Greer, "Metallic glasses as structural materials," Scr. Mater. **54**, 321–326 (2006).
[14]M. Granata, E. Saracco, N. Morgado, A. Cajgfinger, G. Cagnoli, J. Degallaix, V. Dolique, D. Forest, J. Franc, C. Michel *et al.*, "Mechanical loss in state-of-the-art amorphous optical coatings," Phys. Rev. D **93**, 012007 (2016).
[15]J. Schroers, "Processing of bulk metallic glass," Adv. Mater. **22**, 1566–1597 (2010).
[16]G. Kumar, H. X. Tang, and J. Schroers, "Nanomoulding with amorphous metals," Nature **457**, 868 (2009).
[17]R. Li, Z. Chen, A. Datye, G. H. Simon, J. Ketkaew, E. Kinser, Z. Liu, C. Zhou, O. E. Dagdeviren, S. Sohn *et al.*, "Atomic imprinting into metallic glasses," Commun. Phys. **1**, 75 (2018).
[18]M. A. Perez and A. M. Shkel, "Design and demonstration of a bulk micromachined Fabry–Pérot μg-resolution accelerometer," IEEE Sens. J. **7**, 1653–1662 (2007).
[19]A. M. Shkel, "Type I and type II micromachined vibratory gyroscopes," in *2006 IEEE/ION Position, Location, and Navigation Symposium* (IEEE, 2006), pp. 586–593.
[20]M. L. Falk and J. S. Langer, "Dynamics of viscoplastic deformation in amorphous solids," Phys. Rev. E **57**, 7192 (1998).
[21]M. Fan, M. Wang, K. Zhang, Y. Liu, J. Schroers, M. D. Shattuck, and C. S. O'Hern, "Effects of cooling rate on particle rearrangement statistics: Rapidly cooled glasses are more ductile and less reversible," Phys. Rev. E **95**, 022611 (2017).
[22]H. B. Yu, X. Shen, Z. Wang, L. Gu, W. H. Wang, and H. Y. Bai, "Tensile plasticity in metallic glasses with pronounced β relaxations," Phys. Rev. Lett. **108**, 015504 (2012).
[23]M. Fan, K. Zhang, J. Schroers, M. D. Shattuck, and C. S. O'Hern, "Particle rearrangement and softening contributions to the nonlinear mechanical response of glasses," Phys. Rev. E **96**, 032602 (2017).
[24]J. Zemp, M. Celino, B. Schönfeld, and J. F. Löffler, "Crystal-like rearrangements of icosahedra in simulated copper-zirconium metallic glasses and their effect on mechanical properties," Phys. Rev. Lett. **115**, 165501 (2015).
[25]J. Ketkaew, W. Chen, H. Wang, A. Datye, M. Fan, G. Pereira, U. D. Schwarz, Z. Liu, R. Yamada, W. Dmowski *et al.*, "Mechanical glass transition revealed by the fracture toughness of metallic glasses," Nat. Commun. **9**, 3271 (2018).
[26]C. Zener, "Internal friction in solids. I. Theory of internal friction in reeds," Phys. Rev. **52**, 230 (1937).
[27]A. S. Nowick, *Anelastic Relaxation in Crystalline Solids* (Elsevier, 2012), Vol. 1.
[28]M. Barmatz and H. Chen, "Young's modulus and internal friction in metallic glass alloys from 1.5 to 300 K," Phys. Rev. B **9**, 4073 (1974).
[29]Y. Hiki, M. Tanahashi, and S. Takeuchi, "Temperature, frequency, and amplitude dependence of internal friction of metallic glass," J. Non-Cryst. Solids **354**, 994–1000 (2008).
[30]H.-R. Sinning and F. Haeßner, "Influence of the glass transition and crystallization on the internal friction of some metallic glasses," Z. Phys. Chem. **156**, 115–121 (1988).
[31]K. Samwer, R. Rambousky, and M. Moske, "Dynamic mechanical analysis of Zr-AlCu-alloys at and above the glass transition temperature," in *Materials Science Forum* (Trans Tech Publications, 1995), Vol. 179, pp. 761–768.
[32]F. Spaepen, "A microscopic mechanism for steady state inhomogeneous flow in metallic glasses," Acta Metall. **25**, 407–415 (1977).
[33]J. Gilman, "Flow via dislocations in ideal glasses," J. Appl. Phys. **44**, 675–679 (1973).
[34]P. W. Anderson, B. Halperin, and C. M. Varma, "Anomalous low-temperature thermal properties of glasses and spin glasses," Philos. Mag. **25**, 1–9 (1972).
[35]W. Phillips, "Tunneling states in amorphous solids," J. Low Temp. Phys. **7**, 351–360 (1972).
[36]E. Fermi, P. Pasta, S. Ulam, and M. Tsingou, "Studies of the nonlinear problems," Technical Report No. LA-1940, Los Alamos Scientific Laboratory, NM, 1955.
[37]R. Livi, M. Pettini, S. Ruffo, M. Sparpaglione, and A. Vulpiani, "Relaxation to different stationary states in the Fermi-Pasta-Ulam model," Phys. Rev. A **28**, 3544 (1983).
[38]R. Livi, M. Pettini, S. Ruffo, M. Sparpaglione, and A. Vulpiani, "Equipartition threshold in nonlinear large Hamiltonian systems: The Fermi-Pasta-Ulam model," Phys. Rev. A **31**, 1039 (1985).
[39]L. Berchialla, A. Giorgilli, and S. Paleari, "Exponentially long times to equipartition in the thermodynamic limit," Phys. Lett. A **321**, 167–172 (2004).
[40]G. Parisi, "On the approach to equilibrium of a Hamiltonian chain of anharmonic oscillators," Europhys. Lett. **40**, 357 (1997).
[41]G. Benettin, "Time scale for energy equipartition in a two-dimensional FPU model," Chaos **15**, 015108 (2005).
[42]G. Benettin and G. Gradenigo, "A study of the Fermi–Pasta–Ulam problem in dimension two," Chaos **18**, 013112 (2008).
[43]P. Bocchieri, A. Scotti, B. Bearzi, and A. Loinger, "Anharmonic chain with Lennard-Jones interaction," Phys. Rev. A **2**, 2013 (1970).
[44]G. Benettin, G. L. Vecchio, and A. Tenenbaum, "Stochastic transition in two-dimensional Lennard-Jones systems," Phys. Rev. A **22**, 1709 (1980).
[45]G. Benettin and A. Tenenbaum, "Ordered and stochastic behavior in a two-dimensional Lennard-Jones system," Phys. Rev. A **28**, 3020 (1983).
[46]W. Kob and H. C. Andersen, "Testing mode-coupling theory for a supercooled binary Lennard-Jones mixture I: The van Hove correlation function," Phys. Rev. E **51**, 4626 (1995).
[47]J. Wittmer, H. Xu, P. Polińska, F. Weysser, and J. Baschnagel, "Shear modulus of simulated glass-forming model systems: Effects of boundary condition, temperature, and sampling time," J. Chem. Phys. **138**, 12A533 (2013).
[48]A. Tanguy, J. Wittmer, F. Leonforte, and J.-L. Barrat, "Continuum limit of amorphous elastic bodies: A finite-size study of low-frequency harmonic vibrations," Phys. Rev. B **66**, 174205 (2002).
[49]T. Bertrand, C. F. Schreck, C. S. O'Hern, and M. D. Shattuck, "Hypocoordinated solids in particulate media," Phys. Rev. E **89**, 062203 (2014).
[50]H. Mizuno, L. E. Silbert, M. Sperl, S. Mossa, and J.-L. Barrat, "Cutoff nonlinearities in the low-temperature vibrations of glasses and crystals," Phys. Rev. E **93**, 043314 (2016).
[51]H. Chen, H. Leamy, and M. Barmatz, "The elastic and anelastic behavior of a metallic glass," J. Non-Cryst. Solids **5**, 444–448 (1971).
[52]Y. Fan, T. Iwashita, and T. Egami, "How thermally activated deformation starts in metallic glass," Nat. Commun. **5**, 5083 (2014).

[53]H. Sheng, E. Ma, and M. J. Kramer, "Relating dynamic properties to atomic structure in metallic glasses," JOM **64**, 856–881 (2012).
[54]J. Classen, T. Burkert, C. Enss, and S. Hunklinger, "Anomalous frequency dependence of the internal friction of vitreous silica," Phys. Rev. Lett. **84**, 2176 (2000).
[55]A. Fefferman, R. Pohl, A. Zehnder, and J. Parpia, "Acoustic properties of amorphous silica between 1 and 500 mk," Phys. Rev. Lett. **100**, 195501 (2008).
[56]F. Hoehne, Y. A. Pashkin, O. Astafiev, L. Faoro, L. Ioffe, Y. Nakamura, and J. Tsai, "Damping in high-frequency metallic nanomechanical resonators," Phys. Rev. B **81**, 184112 (2010).
[57]P. Poncharal, Z. Wang, D. Ugarte, and W. A. De Heer, "Electrostatic deflections and electromechanical resonances of carbon nanotubes," Science **283**, 1513–1516 (1999).
[58]S. Purcell, P. Vincent, C. Journet, and V. T. Binh, "Tuning of nanotube mechanical resonances by electric field pulling," Phys. Rev. Lett. **89**, 276103 (2002).
[59]V. Khonik, "Internal friction of metallic glasses: Mechanisms and conditions of their realization," J. Phys. IV **6**, C8-591 (1996).
[60]D. Jang and J. R. Greer, "Transition from a strong-yet-brittle to a stronger-and-ductile state by size reduction of metallic glasses," Nat. Mater. **9**, 215 (2010).
[61]I. Issa, L. Joly-Pottuz, J. Réthoré, C. Esnouf, T. Douillard, V. Garnier, J. Chevalier, S. Le Floch, D. Machon, and K. Masenelli-Varlot, "Room temperature plasticity and phase transformation of nanometer-sized transition alumina nanoparticles under pressure," Acta Mater. **150**, 308–316 (2018).
[62]E. Calvié, J. Réthoré, L. Joly-Pottuz, S. Meille, J. Chevalier, V. Garnier, Y. Jorand, C. Esnouf, T. Epicier, J. Quirk *et al.*, "Mechanical behavior law of ceramic nanoparticles from transmission electron microscopy *in situ* nano-compression tests," Mater. Lett. **119**, 107–110 (2014).
[63]J. D. Honeycutt and H. C. Andersen, "Molecular dynamics study of melting and freezing of small Lennard-Jones clusters," J. Phys. Chem. **91**, 4950–4963 (1987).
[64]A. Stukowski, "Visualization and analysis of atomistic simulation data with OVITO–The open visualization tool," Modell. Simul. Mater. Sci. Eng. **18**, 015012 (2009).
[65]E. Schafler, M. Zehetbauer, and T. Ungar, "Measurement of screw and edge dislocation density by means of X-ray Bragg profile analysis," Mater. Sci. Eng.: A **319**, 220–223 (2001).
[66]S. Li, S. Horikawa, M.-k. Park, Y. Chai, V. J. Vodyanoy, and B. A. Chin, "Amorphous metallic glass biosensors," Intermetallics **30**, 80–85 (2012).
[67]J. Schroers, G. Kumar, T. M. Hodges, S. Chan, and T. R. Kyriakides, "Bulk metallic glasses for biomedical applications," JOM **61**, 21–29 (2009).
[68]I. Regev, J. Weber, C. Reichhardt, K. A. Dahmen, and T. Lookman, "Reversibility and criticality in amorphous solids," Nat. Commun. **6**, 8805 (2015).
[69]D. Fiocco, G. Foffi, and S. Sastry, "Encoding of memory in sheared amorphous solids," Phys. Rev. Lett. **112**, 025702 (2014).
[70]P. Leishangthem, A. D. Parmar, and S. Sastry, "The yielding transition in amorphous solids under oscillatory shear deformation," Nat. Commun. **8**, 14653 (2017).
[71]T. Damart, A. Tanguy, and D. Rodney, "Theory of harmonic dissipation in disordered solids," Phys. Rev. B **95**, 054203 (2017).
[72]Q. Wu, T. Bertrand, M. D. Shattuck, and C. S. O'Hern, "Response of jammed packings to thermal fluctuations," Phys. Rev. E **96**, 062902 (2017).